ACS APPLIED MATERIALS & INTERFACES

www.acsami.org Research Article

High-Temperature and Flexible Piezoelectric Sensors for Lamb-Wave-Based Structural Health Monitoring

Xiyuan Zhang, Yu Wang, Xingyao Gao, Yanda Ji, Fengjiao Qian, Jiyu Fan, Haiyan Wang, Lei Qiu,* Weiwei Li,* and Hao Yang*

Cite This: *ACS Appl. Mater. Interfaces* 2021, 13, 47764–47772 **Read Online**

ACCESS | Metrics & More | Article Recommendations | Supporting Information

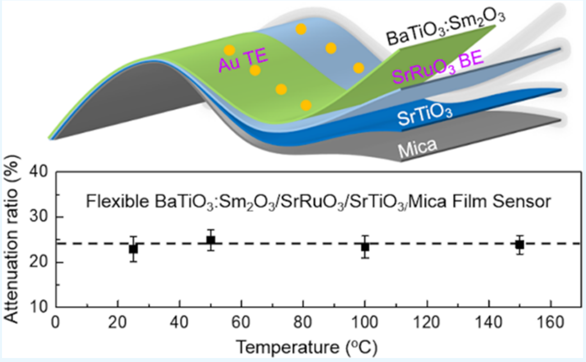

ABSTRACT: Piezoelectric sensors can be utilized in Lamb-wave-based structural health monitoring (SHM), which is an effective method for aircraft structural damage detection. However, due to the inherent stiffness, brittleness, weight, and thickness of piezoelectric ceramics, their applications in aircraft structures with complex curved surfaces are seriously restricted. Herein, we report a flexible, light-weight, and high-performance BaTiO$_3$:Sm$_2$O$_3$/SrRuO$_3$/SrTiO$_3$/mica film sensor that can be used in high-temperature SHM of aircraft. Enhanced ferroelectric Curie temperature (487 °C) and piezoelectric coefficient d_{33} (120−130 pm/V) are achieved in BaTiO$_3$, which can be attributed to the tensile strain developed by stiff Sm$_2$O$_3$ nanopillars. Stable ferroelectricity and piezoelectricity are retained up to 150 °C. The flexible BaTiO$_3$:Sm$_2$O$_3$/SrRuO$_3$/SrTiO$_3$/mica film is validated as an ultrasonic sensor with high sensitivity and stability for damage monitoring on aircraft structures with the curved surface ranging from 25 to 150 °C. Our work demonstrates that flexible and light-weight BaTiO$_3$:Sm$_2$O$_3$/SrRuO$_3$/SrTiO$_3$/mica film sensors can be employed as high-temperature piezoelectric sensors for *real-time* SHM of aircraft structures with complex curved surfaces.

KEYWORDS: *flexible sensor, piezoelectric sensor, BaTiO$_3$, Lamb wave, structural health monitoring*

■ INTRODUCTION

Aircraft structural health monitoring (SHM)[1−6] is an important method for determining the integrity of structures, ensuring flight safety, and guiding the design and maintenance. It utilizes the sensors integrated within aircraft structures to obtain online the structural-health-condition-related signals. This combines signal processing methods, mechanical modeling, and damage diagnosis to evaluate the integrity of structures. Among the existing SHM methods, piezoelectric transducers and the Lamb-wave-based SHM[6−9] method have been widely studied and adopted for their advantages of large monitoring area and high sensitivity to small damage. Apart from carrying out SHM at room temperature, it is of great significance to conduct SHM of curved aircraft structures in a high-temperature environment, such as aircraft engines[10] and engine casings, especially thermal protection systems (TPS)[11−14] of hypersonic aircraft.[11] Due to the harsh and high-temperature flight environment, TPS as well as aircraft structures protected by it may be damaged by the loosening and detachment of connecting bolts, structural cracking, material ablation, etc. This in turn threatens the safety of hypersonic aircraft. Usually, the inner surface temperature of TPS as well as the temperature of structures protected by it is about 150 °C.[14] Currently, to design high-temperature piezoelectric sensors, lead zirconate titanate (PZT) and BaTiO$_3$ ceramics[15,16] as well as composite films prepared by these two materials and other materials[17−23] have been widely studied (Table S1 in the Supporting Information). However, the structure of the inner surfaces of TPS is very complex, and the inherent stiffness, brittleness, thickness, and weight of the piezoelectric ceramics restrict their SHM applications in TPS structures with complex curved surfaces. Therefore, it is still a challenge to realize the high-temperature SHM of complex curved structures. The development of high-temperature piezoelectric sensors with great flexibility and high performance is highly desired.

The existing flexible piezoelectric sensors used for SHM can be divided into three categories (Table S1 in the Supporting Information): poly(vinylidene fluoride) (PVDF) and other related organic piezoelectric materials;[13,24] organic composite piezoelectric materials based on PZT;[17,18] and polycrystalline PZT films based on flexible organic substrates or metal foil substrates.[19,20] Organic, organic composite, and organic

Received: July 20, 2021
Accepted: September 16, 2021
Published: September 28, 2021

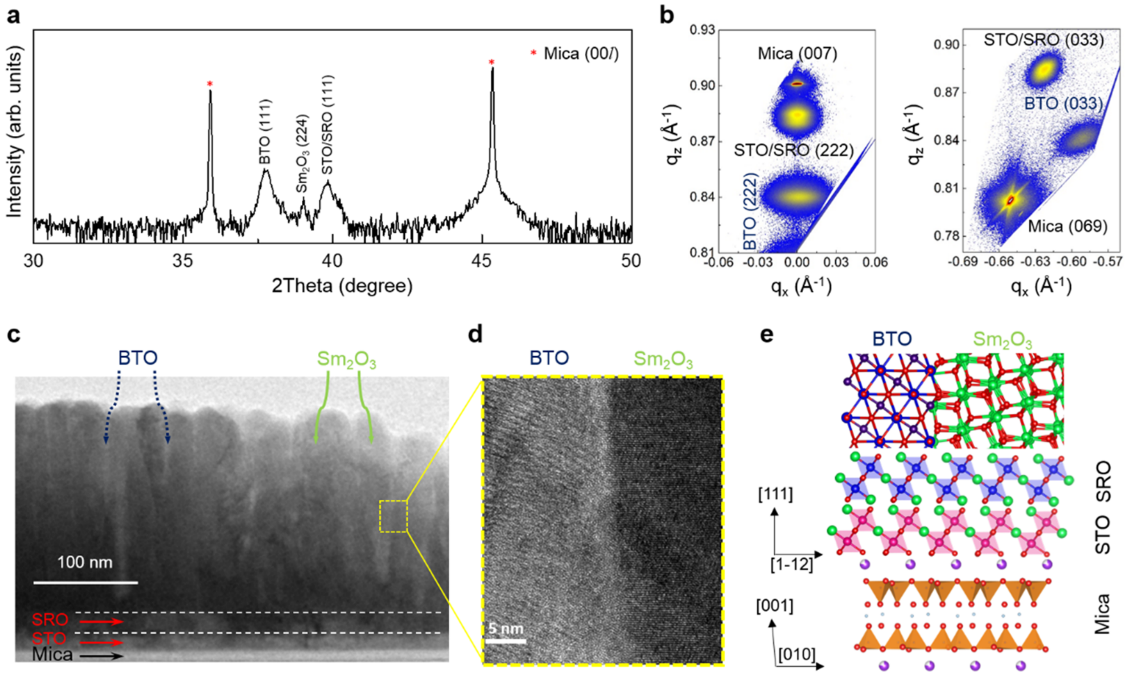

Figure 1. (a) Typical XRD θ−2θ scan of the BTO:Sm_2O_3/SRO/STO/mica film. (b) Reciprocal space maps around mica (007) (left panel) and mica (069) (right panel) peaks. (c) Cross-sectional TEM image showing clear pillars of Sm_2O_3 embedded in a BTO matrix grown on an SRO-STO-buffered mica substrate. (d) High-resolution TEM image of the BTO and Sm_2O_3 interface. (e) Crystallographic model of the BTO:Sm_2O_3/SRO/STO/mica film.

substrate-based flexible piezoelectric sensors used for high-frequency guided wave SHM do not work steadily above room temperature. Regarding piezoelectric film sensors based on metal foil substrates, piezoelectric films need to be transferred/sprayed to metal foil substrates for the realization of flexibility. However, this method requires a complicated process, which is not cost-efficient. On the other hand, metal foil substrates with a thickness of at least millimeter scale are used in sensors. This inevitably brings interference to the reception and interpretation of signals.[25]

Barium titanate ($BaTiO_3$, BTO) and its derivatives can be alternative candidates for designing *lead-free* piezoelectric sensors.[26,27] However, a low Curie temperature of 130 °C in BTO ceramics and a poor piezoelectric coefficient d_{33} (<55 pm/V) in BTO films or nanowires restrict their practical applications around room temperature. Recently, strain engineering has been used for manipulating dielectric properties, improving the leakage current, and enhancing the ferroelectric Curie temperature and polarization in epitaxial BTO films grown on conventional rigid substrates.[28−32] However, these reported piezoelectric properties of epitaxial BTO films are still not comparable to those of PZT films (Table S1 in the Supporting Information).[17−20]

Herein, we report that the flexible BTO:Sm_2O_3/$SrRuO_3$/$SrTiO_3$/mica (BTO:Sm_2O_3/SRO/STO/mica) film can be used as a high-temperature piezoelectric sensor for Lamb-wave-based SHM of complex curved aircraft structures. High-quality BTO:Sm_2O_3 nanocomposite films with the thickness of 500 nm were grown on SRO-STO-buffered inorganic muscovite mica, $KAl_2(AlSi_3O_{10})F_2$, substrates through the van der Waals (vdW) epitaxy.[33−36] Enhanced ferroelectric Curie temperature, from 130 to 487 °C, and piezoelectric coefficient d_{33} (120−130 pm/V) are achieved in the BTO *via* strain engineering. The change in the piezoelectric coefficient d_{33} and the dielectric constant is below 4% by varying the temperature from 25 to 150 °C. In addition, the piezoelectricity and flexibility of the flexible BTO:Sm_2O_3/SRO/STO/mica film sensor remain excellent after 10^4 bending cycles. By comparing the change in amplitudes of the health-response signals and damage-response signals on the curved aluminum plate, from 25 to 150 °C, the stable attenuation ratio was around 23.9%. Our work demonstrates that the flexible BTO:Sm_2O_3/SRO/STO/mica film sensor can be applied as a high-temperature piezoelectric sensor for *real-time* Lamb-wave-based SHM of both flat and curved platelike structures.

RESULTS AND DISCUSSION

The X-ray diffraction (XRD) θ−2θ scan of the BTO:Sm_2O_3 nanocomposite film reveals that only (111) BTO, SRO, and STO and (224) Sm_2O_3 diffraction peaks with mica (00*l*) peaks can be observed without any other intermixed crystalline phases (Figure 1a). The XRD spectrum also confirms that BTO and Sm_2O_3 phases coexist in the nanocomposite film, consistent with previous reports.[29,30] In comparison with the pure BTO film (Figure S1 in the Supporting Information), we found that the peak position of BTO (111) in the BTO:Sm_2O_3 nanocomposite film clearly shifts toward a lower angle. This indicates that the BTO phase in the BTO:Sm_2O_3 nanocomposite film is under tensile strain along the out-of-plane direction. The lattice constant of the BTO (222) peak is increased to be around 1.1905 Å (1.1601 Å for the bulk BTO (222) peak). Based on the equation of $\frac{1.1905 - 1.1601}{1.1601}$%, the out-of-plane tensile strain is calculated to be ∼2.62% for the BTO phase in the BTO:Sm_2O_3 nanocomposite film. According to previous reports,[30,32] the observed tensile strain in BTO is induced by the lattice mismatch with the stiff Sm_2O_3 phase, which is insulating (nonferroelectric material) and has a large elastic modulus of 125 GPa, compared to 67 GPa of BTO.[37,38]

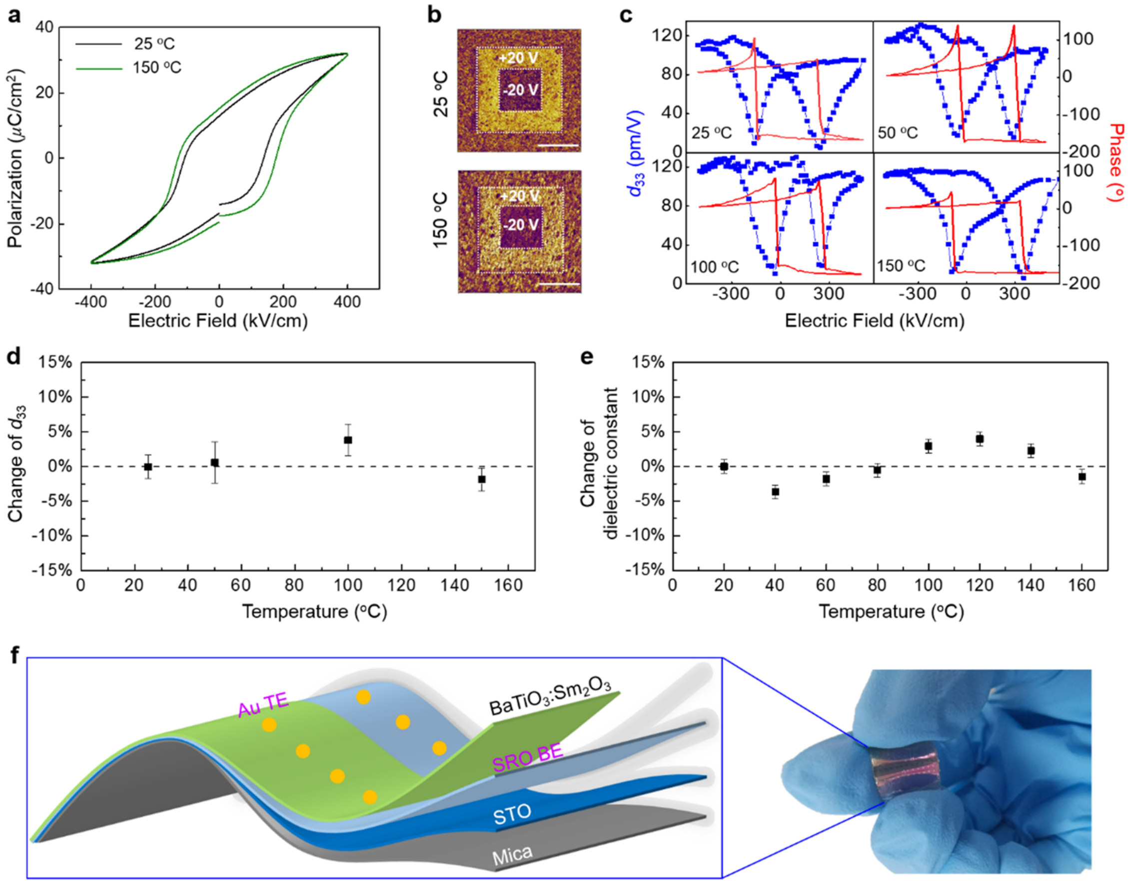

Figure 2. (a) Ferroelectric hysteresis loops. (b) PFM phase contrast after + 20 V writing (10 × 10 μm^2) and −20 V writing (5 × 5 μm^2). Scale bar is 5 μm. (c) Effective piezoelectric coefficient d_{33} and phase hysteresis loops. Temperature-dependent changes of (d) the effective piezoelectric coefficient d_{33} and (e) the dielectric constant. Room-temperature values are the reference. (f) Left panel: schematic diagram of the flexible BTO:Sm_2O_3/SRO/STO/mica film sensor used for Lamb-wave measurements. TE and BE are top and bottom electrodes, respectively. Right panel: photograph of the flexible BTO:Sm_2O_3/SRO/STO/mica film sensor under bending with a 15 μm thick mica cleavage.

X-ray reciprocal space maps (RSMs) were used to determine the crystallographic orientation along the in-plane direction (Figure 1b). The detailed microstructure of the BTO:Sm_2O_3/SRO/STO nanocomposite film was further investigated by a transmission electron microscope (TEM) (Figure 1c), revealing the layered structure of the BTO:Sm_2O_3/SRO/STO/mica. Also, we can see that self-assembled Sm_2O_3 nanopillars are distributed and embedded in a BTO matrix.[29,30,32] High-resolution TEM image (Figure 1d) exhibits a defect-free and coherent interface at the interface between BTO and Sm_2O_3. Based on XRD and TEM results, high-quality heteroepitaxy of the BTO:Sm_2O_3/SRO/STO film on flexible mica substrates is delivered, as shown in Figure 1e.

Owing to the large tensile strain applied to BTO in the nanocomposite film, its ferroelectric and piezoelectric properties are strongly improved. Compared with the ferroelectric Curie temperature of 130 °C for the BTO ceramic, the ferroelectric Curie temperature of BTO in the nanocomposite film enhanced to around 487 °C (Figure S2 in the Supporting Information), in agreement with the theoretical prediction.[39] Moreover, as shown in Figure 2a, robust ferroelectric hysteresis loops were measured from 25 to 150 °C, indicating that ferroelectricity can be retained in the flexible BTO:Sm_2O_3/SRO/STO/mica film at least at 150 °C. This is further confirmed by the box-in-box phase mapping through piezoresponse force microscopy (PFM) measurements (Figure 2b). In addition, the piezoelectric properties of the flexible BTO:Sm_2O_3/SRO/STO/mica film with a 15 μm thick mica substrate were systematically investigated by PFM (Figure 2c). The piezoelectric coefficient (d_{33}) with an enhanced value of 120−130 pm/V is attributed to the tensile strain generated by the rigid Sm_2O_3 nanopillars.[40] Moreover, it is retained from 25 to 150 °C. The d_{33} value of this work (Table S1 in the Supporting Information) is higher than that of BTO nanowires, plain BTO films, and BTO:Sm_2O_3 nanocomposite films grown on conventional rigid substrates.[22,23,41] We also noted that the piezoelectric coefficient (d_{33}) of the flexible BTO:Sm_2O_3/SRO/STO/mica film is comparable to that of PZT films.[21] Furthermore, a decent stability of piezoelectricity and flexibility was confirmed by 10^4 bending cycles (Figure S3 in the Supporting Information). This indicates that a flexible BTO:Sm_2O_3/SRO/STO/mica film can be a candidate for developing a *lead-free* and light-weight piezoelectric sensor. Also, as shown in Figure 2d,e, temperature-dependent changes of d_{33} and the dielectric constant are below 4%. High-temperature stability of d_{33} and the dielectric constant observed in the flexible BTO:Sm_2O_3/SRO/STO/mica film is pivotal to the development of a high-temperature piezoelectric sensor. Figure 2f exhibits the schematic diagram and photographic image of the flexible BTO:Sm_2O_3/SRO/STO/mica film sensor used for Lamb-wave-based SHM measurements.

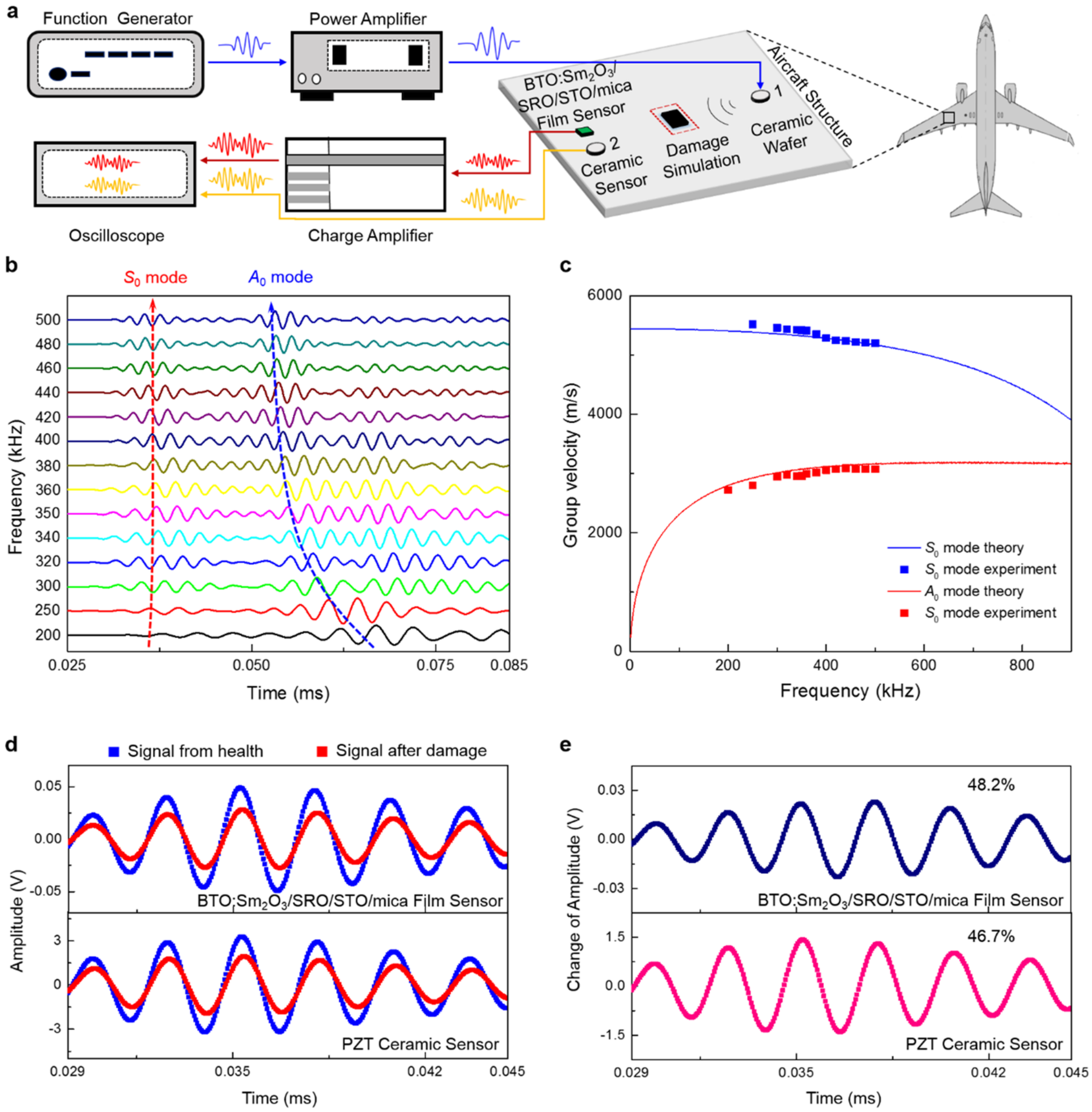

Figure 3. (a) Schematic diagram of the experimental setup for measuring Lamb-wave response signals. (b) Lamb-wave response signals at different central frequencies measured from the flat aluminum plate and at 25 °C. (c) Comparison of the group velocities of S_0 and A_0 modes of experimental and theoretical results. (d) S_0 mode of Lamb-wave response signals at a central frequency of 350 kHz detected by the flexible BTO:Sm$_2$O$_3$/SRO/STO/mica film sensor (top panel) and the PZT ceramic (bottom panel) sensor and measured at 25 °C. (e) Change in amplitude of Lamb-wave response signals in the S_0 mode for the flexible BTO:Sm$_2$O$_3$/SRO/STO/mica film sensor (top panel) and the PZT ceramic (bottom panel) sensor obtained from (d).

To verify that the flexible BTO:Sm$_2$O$_3$/SRO/STO/mica film sensor can correctly respond to Lamb wave and can be applied to high-temperature SHM of complex curved structures, three experiments were carried out, including Lamb-wave response and damage monitoring on an aluminum flat-plate, damage monitoring on an aluminum plate with a complex curved surface, and high-temperature damage monitoring on an aluminum plate with a complex curved surface.

Figure 3a presents an enlarged schematic diagram of the SHM experiment of an aluminum flat-plate structure of aircraft. The flexible BTO:Sm$_2$O$_3$/SRO/STO/mica film sensor (10 mm × 5 mm × 500 nm) and the PZT 5A ceramic wafer (PZT 1, φ 8 mm × 0.48 mm, Fuji Ceramics Corporation) were pasted on the 2 mm thick aluminum flat-plate as the sensing element and the actuating element, respectively. Another PZT 5A ceramic wafer (PZT 2, φ 8 mm × 0.48 mm, Fuji Ceramics Corporation) as a reference sensing element was also pasted next to the flexible BTO:Sm$_2$O$_3$/SRO/STO/mica film sensor. It should be emphasized that the weight of one flexible BTO:Sm$_2$O$_3$/SRO/STO/mica film sensor is around 2.9 mg, which is significantly lighter than that of one commercial PZT 5A ceramic wafer (φ 8 mm × 0.48 mm, Fuji Ceramics Corporation) with the weight of 170 mg. This demonstrates the advantage of the flexible BTO:Sm$_2$O$_3$/SRO/STO/mica film sensor in being light weight. The distance between the excitation source and the sensing elements was 15 cm. The five-peak wave signals with different central frequencies were generated by a function generator and amplified to ±70 V by a power amplifier and then applied to the PZT 1 (excitation source). Based on the inverse piezoelectric effect, the deformation of the PZT ceramic wafer causes the Lamb wave to be excited and propagated along the aluminum flat-plate. By utilizing the

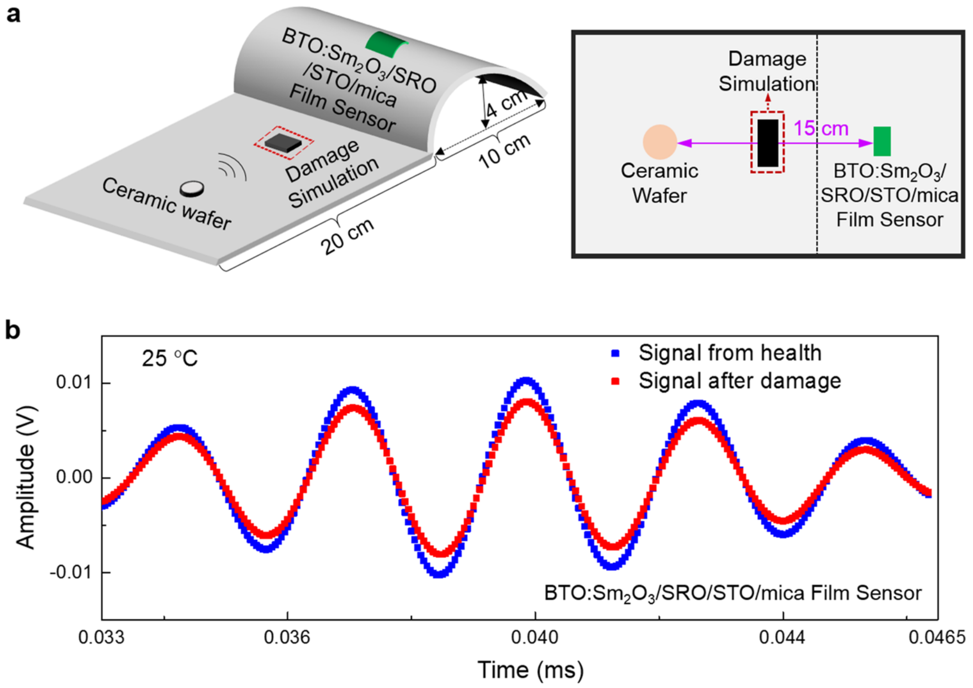

Figure 4. (a) Side view (left panel) and top view (right panel) of the schematic diagram of detecting damage on the curved aluminum plate. (b) S_0 mode of Lamb-wave response signals at a central frequency of 350 kHz received by the flexible BTO:Sm$_2$O$_3$/SRO/STO/mica film sensor.

positive piezoelectric effect, the flexible BTO:Sm$_2$O$_3$/SRO/STO/mica film sensor and PZT 2 converted the deformation caused by Lamb wave into electrical signals, which were amplified by 50 times using a charge amplifier and eventually displayed on an oscilloscope (Figure 3a).

The waterfall plot of Lamb-wave response signals received by the flexible BTO:Sm$_2$O$_3$/SRO/STO/mica film sensor is presented in Figure 3b, which was obtained by sweeping the frequency without damage simulation. Each line represents a response signal at a central frequency ranging from 200 to 500 kHz. Among the response signals, the relative signal amplitudes of S_0 and A_0 modes are different by sweeping the frequency. At low frequencies, the response signal amplitude of the S_0 mode is very small compared with that of the A_0 mode. With the increase in frequency, the response signal amplitude of the S_0 mode becomes larger and both A_0 and S_0 modes start to be activated.[7] Furthermore, group velocities of A_0 and S_0 modes of experimental results at different frequencies are calculated and compared with the theoretical dispersion curve of the Lamb wave on the 2 mm thick aluminum flat-plate (Figure 3c). We can see that group velocities of the experimental results agree well with theoretical values, and the group velocities of S_0 and A_0 modes become smaller and larger, respectively, with the increase of frequency. These prove the correctness of Lamb-wave response signals received by the flexible BTO:Sm$_2$O$_3$/SRO/STO/mica film sensor. The amplitude and waveform of the Lamb wave with the central frequency of 350 kHz are the most stable, and the influence of boundary scattering is the least. Thus, the S_0 mode of the Lamb wave of 350 kHz is selected as subsequent damage detection experiments.

To further investigate the response of the flexible BTO:Sm$_2$O$_3$/SRO/STO/mica film sensor to damages, following the method developed by Sohn et al.,[42] a soft sealant used as an artificial damage was bonded on the aluminum plate for simulating the real damage (Figure 3a). Theoretically, the response signal amplitude of the Lamb wave will decrease obviously after the occurrence of damage.[43−45] Figure 3d displays the Lamb-wave response signals received by the flexible BTO:Sm$_2$O$_3$/SRO/STO/mica film sensor and PZT 2 before and after the damage simulation. Basically, the S_0 modes of the Lamb-wave response signals received by the flexible BTO:Sm$_2$O$_3$/SRO/STO/mica film sensor and PZT 2 in a healthy state are consistent, except for the difference in signal amplitude and time. This is caused by the difference in the volume and mass of the film and the ceramic and the difference in their piezoelectric properties. On the other hand, after the damage simulation, the amplitude of Lamb wave response signal detected by flexible BTO:Sm$_2$O$_3$/SRO/STO/mica film sensor is significantly weaker than that of Lamb wave response signal before the damage simulation. A similar attenuation of the amplitude of the Lamb-wave response signal was also detected by PZT 2. The change in amplitude of response signals before and after the damage event is presented in Figure 3e. The average amplitude of the six peaks of response signals after the damage event received by the flexible BTO:Sm$_2$O$_3$/SRO/STO/mica film sensor and PZT 2 decreased by 48.2 and 46.7%, respectively. This indicates that the sensitivity of the flexible BTO:Sm$_2$O$_3$/SRO/STO/mica film sensor is slightly better than that of the PZT ceramic sensor. These results also demonstrate that the flexible BTO:Sm$_2$O$_3$/SRO/STO/mica film sensor may replace the role of the PZT ceramic sensor in Lamb-wave-based damage detection. We want to emphasize that the flexible BTO:Sm$_2$O$_3$/SRO/STO/mica film sensor has the characteristics of being *lead-free*, light weight, and flexible.

Thanks to its light weight and flexibility, the flexible BTO:Sm$_2$O$_3$/SRO/STO/mica film sensor can overcome some disadvantages of the PZT ceramic sensor and be mounted on complex structures with curved surfaces. The side view and top view of the schematic diagram of detecting damage on the curved aluminum plate are provided in Figure 4a. The flexible BTO:Sm$_2$O$_3$/SRO/STO/mica film sensor as

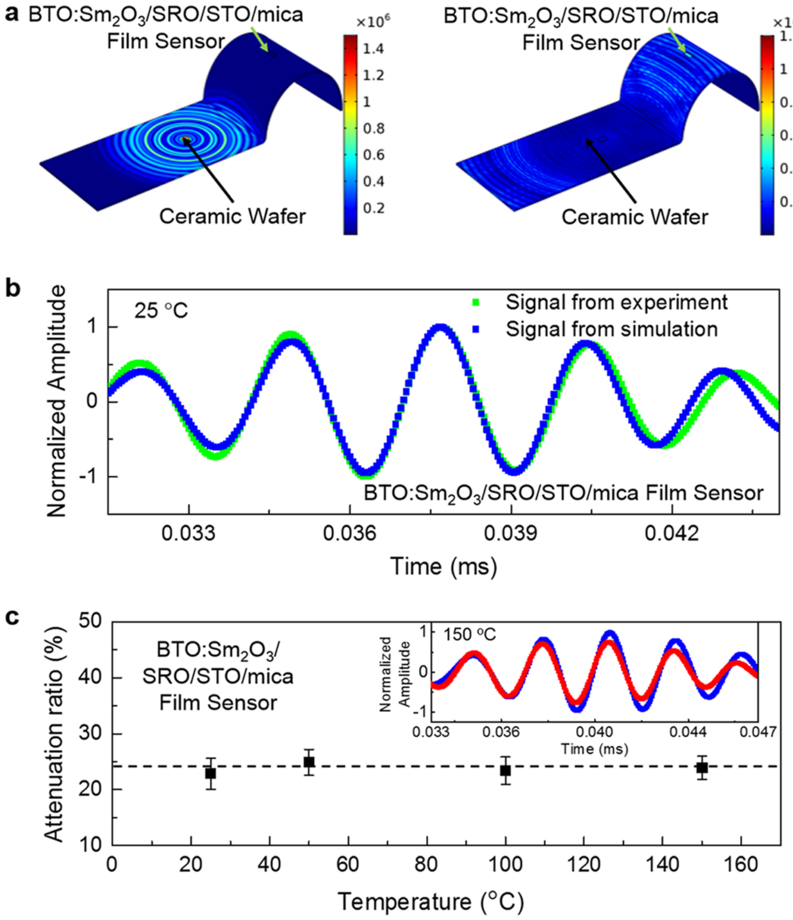

Figure 5. (a) Dynamic Lamb waves excited at 0.02 ms (left panel) and received at 0.04 ms (right panel). (b) Comparison of the S_0 mode of Lamb-wave response signals at a central frequency of 350 kHz obtained from the simulation and experiment. (c) Temperature-dependent attenuation ratio calculated from the change in amplitude of Lamb-wave response signals in the S_0 mode for the flexible BTO:Sm$_2$O$_3$/SRO/STO/mica film sensor. The inset is the S_0 mode of Lamb-wave response signals at a central frequency of 350 kHz measured at 150 °C. The blue wave indicates signal from health, and the red wave indicates signal after damage.

the sensing element was mounted on the curved part of the aluminum plate, while the PZT ceramic wafer as the excitation source was attached to the flat part of the aluminum plate. The curvature of the bonding position of the flexible BTO:Sm$_2$O$_3$/SRO/STO/mica film sensor is around 0.016 mm^{-1}. The distance between the flexible BTO:Sm$_2$O$_3$/SRO/STO/mica film sensor and the PZT ceramic is still 15 cm. Similar to the SHM experiment on an aluminum flat-plate, an artificial damage case was bonded on the flat part of the aluminum plate to simulate the real damage. Lamb-wave response signals were acquired before and after the damage simulation. The excitation signal was still amplified by ±70 V with wave signals at a 350 kHz central frequency. As shown in Figure 4b, the amplitudes of Lamb-wave response signals are significantly decreased after the damage simulation. Due to the high signal-to-noise ratio, the flexible BTO:Sm$_2$O$_3$/SRO/STO/mica film sensor accurately extracted the damage reading.

To validate the correctness of Lamb-wave response signals of the flexible BTO:Sm$_2$O$_3$/SRO/STO/mica film sensor on the curved aluminum plate, the finite element simulation (FEM) analysis of Lamb-wave propagation on an aluminum plate based on the flexible BTO:Sm$_2$O$_3$/SRO/STO/mica film sensor was carried out (Figure S4 in the Supporting Information). Figure 5a presents the dynamic Lamb waves excited at 0.02 ms and received at 0.04 ms. Lamb waves are indeed transferred through the curved surface and received by the flexible BTO:Sm$_2$O$_3$/SRO/STO/mica film sensor. Lamb-wave response signals obtained from the experiment and simulation are further compared and shown in Figure 5b. The response signals are normalized by amplitude and aligned by the peak value for easy comparison. Obviously, the S_0 mode of the simulation signal agrees well with that of the experimental signal, which proves the correctness of the experimental signal. These results strongly suggest that the flexible BTO:Sm$_2$O$_3$/SRO/STO/mica film sensor can achieve damage monitoring on the curved aluminum plate.

To further examine the stability and reliability of the flexible BTO:Sm$_2$O$_3$/SRO/STO/mica film sensor working at a high temperature, we carried out the experiment of high-temperature damage monitoring on an aluminum plate with a curved surface. The aluminum plate with the flexible BTO:Sm$_2$O$_3$/SRO/STO/mica film sensor mounted on the curved part and the PZT ceramic wafer mounted on the flat part was placed in a chamber by changing the temperature from 25 to 150 °C (maximum temperature of the chamber). The high-temperature experiment was carried out at 150 °C for more than 2 h without signal attenuation or abnormality. Accordingly, signal wires and the binder were replaced by ones that can withstand high temperatures. The inset of Figure 5c shows the comparison of Lamb-wave response signals received by the flexible BTO:Sm_2O_3/SRO/STO/mica film sensor and measured at 150 °C before and after the damage simulation. The amplitude of the Lamb-wave response signal is clearly found to decrease after the damage simulation. More importantly, as presented in Figure 5c, the attenuation ratio calculated from the change in amplitude of Lamb-wave response signals stabilizes at around 23.9% by varying the temperature from 25 to 150 °C. These results demonstrate that the flexible BTO:Sm_2O_3/SRO/STO/mica film sensor shows excellent stability and reliability at high temperatures.

■ CONCLUSIONS

In summary, an enhancement of the ferroelectric Curie temperature (487 °C) and the piezoelectric coefficient (d_{33}) with a value of 120−130 pm/V is achieved in the flexible BTO:Sm_2O_3/SRO/STO/mica film owing to the tensile strain induced by the stiff Sm_2O_3 nanopillars. The stability of d_{33} and the dielectric constant is confirmed by varying the temperature from 25 to 150 °C. Lamb-wave-based damage monitoring on both flat and curved aluminum plates is demonstrated by the flexible BTO:Sm_2O_3/SRO/STO/mica film sensor. More importantly, the flexible BTO:Sm_2O_3/SRO/STO/mica film sensor shows a high sensitivity and stability of detecting damages from 25 to 150 °C on the curved aluminum plate. Our work demonstrates the feasibility of employing the flexible BTO:Sm_2O_3/SRO/STO/mica film sensor as a high-temperature piezoelectric sensor with characteristics of being *lead-free* and light weight for *real-time* online SHM of aircraft structures with complex curved surfaces.

■ EXPERIMENTAL SECTION

Film Fabrication. $(BaTiO_3)_{0.5}$:$(Sm_2O_3)_{0.5}$ nanocomposite films and $BaTiO_3$ films were deposited on mica substrates using pulsed laser deposition. The growth temperature was at 800 °C, and the oxygen partial pressure was optimized at 0.25 mbar with a laser repetition rate of 3 Hz. Prior to the growth of $(BaTiO_3)_{0.5}$:$(Sm_2O_3)_{0.5}$ nanocomposite films, the $SrTiO_3$ buffer layer and the $SrRuO_3$ electrode layer were deposited at 780 °C with 0.2 mbar oxygen partial pressure. After the deposition, all films were cooled at a rate of 5 °C/min to room temperature in an oxygen pressure of 0.8 atm. Mica substrates were exfoliated to a thickness of 15 μm by mechanical stripping, which allowed the $(BaTiO_3)_{0.5}$:$(Sm_2O_3)_{0.5}$ nanocomposite film to bend.

Characterization. High-resolution four-circle X-ray diffraction (Panalytical Empyrean, Kα radiation) and transmission electron microscopy (TEM, FEI Tecnai F20 analytical microscopy) were used to investigate the crystallography of thin films. Piezoresponse force microscopy measurements were carried out using Asylum Research AFM MFP-3D origin with an environmental controller and an HVA 220 high-voltage amplifier. To obtain the deformation of the piezoelectric material due to the application of voltage, the switching spectroscopy PFM (SS-PFM)[46,47] was conducted to determine the measured piezoresponse amplitude as a function of driving frequency, f

$$A(f) = \frac{f_0^2 A_d}{\sqrt{(f_0^2 - f^2)^2 + (f_0 f/Q)^2}} \quad (1)$$

where A_d is the amplitude of the electric-field-induced deformation driving the system, Q is the quality factor, and f_0 is the resonant frequency. In addition, SS-PFM measurements were performed in the dual AC resonance tracking (DART) mode, which used two excitation frequencies f_1 and f_2 and led to four measured quantities, namely, the corresponding amplitudes A_1 and A_2 and phases Φ_1 and Φ_2. As a result, the A_d can be calculated from the obtained values of Q and f_0. The effective piezoelectric coefficient d_{33}^{eff} was further extracted from $A_d = d_{33}^{eff}V_{ac}$, where V_{ac} is a drive amplitude. Ferroelectric hysteresis loops were measured by a Radiant Precision materials analyzer. Dielectric measurements were carried out using an impedance analyzer (E4990A). The temperature was controlled by a Linkam Scientific Instruments HFS600E-PB4 system. For the ferroelectric and dielectric measurements, Au top electrodes with an area of 7.85 × 10^{-5} cm^2 were used. The instrument used for bending is a lab-made oscillator, and a bending radius of 4 mm was used for examining the flexibility.

SHM Measurements. To carry out the SHM on the aluminum plate, the flexible $(BaTiO_3)_{0.5}$:$(Sm_2O_3)_{0.5}$/$SrRuO_3$/$SrTiO_3$/mica film was processed as a sensor. The $SrRuO_3$ layer is the bottom electrode, and the Au top electrode with an area of 7.065 × 10^{-2} cm^2 is sputtered onto the flexible $(BaTiO_3)_{0.5}$:$(Sm_2O_3)_{0.5}$/$SrRuO_3$/$SrTiO_3$/mica film, forming a typical sandwich structure sensor (Figure 2f). Indium was used to weld the film to the shielding wire and eventually to connect it to the measurement system, which includes a digital storage oscilloscope (Agilent MSOX 3014A), a function generator (SDG 5122), a power amplifier (KROHN-HITE MODEL 7602M), and a charger amplifier (homemade). To conduct SHM above room temperature, a high-temperature test chamber (PV-221CSB) was used to control the temperature from 25 to 150 °C. The heating rate was 5 °C/min, and the duration was 30 mins for each tested temperature, which guarantees the stability of temperature and the durability of the flexible $(BaTiO_3)_{0.5}$:$(Sm_2O_3)_{0.5}$/$SrRuO_3$/$SrTiO_3$/mica film sensor.

■ ASSOCIATED CONTENT

Supporting Information

The Supporting Information is available free of charge at https://pubs.acs.org/doi/10.1021/acsami.1c13704.

> Additional XRD θ−2θ patterns; temperature-dependent dielectric permittivity; flexible characteristic diagram; method and geometric model for FEM simulation; and comparison of flexibility, piezoelectric coefficient (d_{33}), working temperature, and Curie temperature of sensors (PDF)

■ AUTHOR INFORMATION

Corresponding Authors

Lei Qiu − *Research Center of Structural Health Monitoring and Prognosis, State Key Laboratory of Mechanics and Control of Mechanical Structures, Nanjing University of Aeronautics and Astronautics, Nanjing 210016, China;* Email: lei.qiu@nuaa.edu.cn

Weiwei Li − *College of Science, Nanjing University of Aeronautics and Astronautics, Nanjing 211106, China; MIIT Key Laboratory of Aerospace Information Materials and Physics, Nanjing University of Aeronautics and Astronautics, Nanjing 211106, China; Department of Materials Science & Metallurgy, University of Cambridge, Cambridge CB3 0FS, U.K.;* orcid.org/0000-0001-5781-5401; Email: wl337@nuaa.edu.cn

Hao Yang − *College of Science, Nanjing University of Aeronautics and Astronautics, Nanjing 211106, China; MIIT Key Laboratory of Aerospace Information Materials and Physics, Nanjing University of Aeronautics and Astronautics, Nanjing 211106, China;* Email: yanghao@nuaa.edu.cn

Authors

Xiyuan Zhang − *College of Science, Nanjing University of Aeronautics and Astronautics, Nanjing 211106, China; MIIT Key Laboratory of Aerospace Information Materials and Physics, Nanjing University of Aeronautics and Astronautics, Nanjing 211106, China; Center of*

Experimental Physics, High Energy Physics Chinese Academy of Sciences, Beijing 100049, China
Yu Wang − *Research Center of Structural Health Monitoring and Prognosis, State Key Laboratory of Mechanics and Control of Mechanical Structures, Nanjing University of Aeronautics and Astronautics, Nanjing 210016, China*
Xingyao Gao − *School of Materials Engineering, Purdue University, West Lafayette, Indiana 47907, United States*
Yanda Ji − *College of Science, Nanjing University of Aeronautics and Astronautics, Nanjing 211106, China; MIIT Key Laboratory of Aerospace Information Materials and Physics, Nanjing University of Aeronautics and Astronautics, Nanjing 211106, China*
Fengjiao Qian − *College of Science, Nanjing University of Aeronautics and Astronautics, Nanjing 211106, China; MIIT Key Laboratory of Aerospace Information Materials and Physics, Nanjing University of Aeronautics and Astronautics, Nanjing 211106, China*
Jiyu Fan − *College of Science, Nanjing University of Aeronautics and Astronautics, Nanjing 211106, China; MIIT Key Laboratory of Aerospace Information Materials and Physics, Nanjing University of Aeronautics and Astronautics, Nanjing 211106, China;* orcid.org/0000-0001-6698-6384
Haiyan Wang − *School of Materials Engineering, Purdue University, West Lafayette, Indiana 47907, United States;* orcid.org/0000-0002-7397-1209

Complete contact information is available at: https://pubs.acs.org/10.1021/acsami.1c13704

Author Contributions

X.Z. and Y.W. contributed equally to this work. H.Y., L.Q., and W.L. supervised the project. X.Z fabricated the samples and carried out the XRD, piezoelectric, and ferroelectric measurements with support from Y.J., F.Q., and J.F. Y.W. and L.Q. carried out the measurement and the simulation of the SHM system. X.G. and H.W. performed the STEM measurements. X.Z., Y.W., W.L., L.Q., and H.Y. prepared the manuscript with contribution from all authors.

Notes

The authors declare no competing financial interest.

■ ACKNOWLEDGMENTS

This work was supported by the National Nature Science Foundation of China (Grant Nos. 11774172, 11974181, 51635007, and 51975292) and the China Scholarship Council (File No. 201906830034). W.L. acknowledges support from the National Natural Science Foundation of China (Grant No. 52102177), the National Natural Science Foundation of Jiangsu Province (Grant No. BK20210313), and Top-notch Academic Programs Project of Jiangsu Higher Education Institutions (TAPP). W.L. also acknowledges support from the Jiangsu Specially-Appointed Professor Program. X.G. and H.W. acknowledge the support from the U.S. National Science Foundation (DMR-1565822 and 1809520) for the high-resolution TEM and STEM effort.

■ REFERENCES

(1) Giurgiutiu, V.; Zagrai, A.; Bao, J. J. Piezoelectric Wafer Embedded Active Sensors for Aging Aircraft Structural Health Monitoring. *Struct. Health Monit.* **2002**, *1*, 41−61.

(2) Ihn, J. B.; Chang, F. K. Pitch-catch Active Sensing Methods in Structural Health Monitoring for Aircraft Structures. *Struct. Health Monit.* **2008**, *7*, 5−19.

(3) Qiu, L.; Yuan, S.; Zhang, X.; Wang, Y. A Time Reversal Focusing Based Impact Imaging Method and Its Evaluation on Complex Composite Structures. *Smart Mater. Struct.* **2011**, *20*, No. 105014.

(4) Foote, P. D. Integration of Structural Health Monitoring Sensors with Aerospace, Composite Materials and Structures. *Materialwiss. Werkstofftech.* **2015**, *46*, 197−203.

(5) Yuan, S.; Ren, Y.; Qiu, L.; Mei, H. A Multi-Response-Based Wireless Impact Monitoring Network for Aircraft Composite Structures. *IEEE Trans. Ind. Electron.* **2016**, *63*, 7712−7722.

(6) Qing, X. L.; Li, W. Z.; Wang, Y. S.; Sun, H. Piezoelectric Transducer-Based Structural Health Monitoring for Aircraft Applications. *Sensors* **2019**, *19*, 545.

(7) Giurgiutiu, V. Tuned Lamb Wave Excitation and Detection with Piezoelectric Wafer Active Sensors for Structural Health Monitoring. *J. Intell. Mater. Syst. Struct.* **2005**, *16*, 291−305.

(8) Su, Z.; Ye, L.; Lu, Y. Guided Lamb Waves for Identification of Damage in Composite Structures: A Review. *J. Sound Vib.* **2006**, *295*, 753−780.

(9) Mitra, M.; Gopalakrishnan, S. Guided Wave Based Structural Health Monitoring: A Review. *Smart Mater. Struct.* **2016**, *25*, No. 053001.

(10) Hoshyarmanesh, H.; Ghodsi, M.; Kim, M.; Cho, H.; Park, H. Temperature Effects on Electromechanical Response of Deposited Piezoelectric Sensors Used in Structural Health Monitoring of Aerospace Structures. *Sensors* **2019**, *19*, 2805.

(11) Kundu, T.; Das, S.; Jata, K. V. Health Monitoring of a Thermal Protection System Using Lamb Waves. *Struct. Health Monit.* **2009**, *8*, 29−45.

(12) Yang, J. Y.; Chang, F. K. Detection of Bolt Loosening in C-C Composite Thermal Protection Panels: I. Diagnostic Principle. *Smart Mater. Struct.* **2006**, *15*, No. 581.

(13) Ting, Y.; Nugraha, A.; Chiu, C. W.; Gunawan, H. Design and Characterization of One-layer PVDF Thin Film for a 3D Force Sensor. *Sens. Actuators, A* **2016**, *250*, 129.

(14) Blosser, M. L. Development of Metallic Thermal Protection Systems for the Reusable Launch Vehicle. *AIP Conf. Proc.* **1997**, *387*, 1125−1144.

(15) Kim, B. J.; Park, T. G.; Kim, M. H. Temperature and Frequency Dependence of Dielectric Properties of (Ba,Sr,Mg)TiO_3 Ceramics Capacitors. *J. Korean Phys. Soc.* **1998**, *32*, 289−291.

(16) Schulz, M. J.; Sundaresan, M. J.; Mcmichael, J.; Clayton, D.; Sadler, R.; Nagel, B. Piezoelectric Materials at Elevated Temperature. *J. Intell. Mater. Syst. Struct.* **2003**, *14*, 693.

(17) Sappati, K. K.; Bhadra, S. Printed Acoustic Sensor for Low Concentration Volatile Organic Compound Monitoring. *IEEE Sens. J.* **2021**, *21*, 9808−9818.

(18) Du, W.; Hoyt, J.; Williams, N.; Cook-Chennault, K. A. The Influence of Processing Parameters on Piezoelectric and Dielectric Properties of Dome-Shaped Composite PZT-epoxy Actuators. *J. Manuf. Process.* **2020**, *57*, 48−60.

(19) Qi, Y.; Kim, J.; Nguyen, T. D.; Lisko, B.; Purohit, P. K.; McAlpine, M. C. Enhanced Piezoelectricity and Stretchability in Energy Harvesting Devices Fabricated from Buckled PZT Ribbons. *Nano Lett.* **2011**, *11*, 1331−1336.

(20) Liang, R. J.; Wang, Q. M. High Sensitivity Piezoelectric Sensors Using Flexible PZT Thick-film for Shock Tube Pressure Testing. *Sens. Actuators, A* **2015**, *235*, 317−327.

(21) Hoshyarmanesh, H.; Ebrahimi, N.; Jafari, A.; Hoshyarmanesh, P.; Kim, M.; Park, H. PZT/PZT and PZT/BiT Composite Piezo-Sensors in Aerospace SHM Applications: Photochemical Metal Organic + Infiltration Deposition and Characterization. *Sensors* **2019**, *19*, 13.

(22) Zhou, Z.; Tang, H.; Sodano, H. A. Vertically Aligned Arrays of $BaTiO_3$ Nanowires. *ACS Appl. Mater. Interfaces* **2013**, *5*, 11894−11899.

(23) Kim, I.; Avrahami, Y.; Tuller, H. L.; et al. Study of Orientation Effect on Nanoscale Polarization in $BaTiO_3$ Thin Films Using Piezoresponse Force Microscopy. *Appl. Phys. Lett.* **2005**, *86*, No. 192907.

(24) Kechiche, M. B.; Bauer, F.; Harzallah, O.; Drean, J. Y. Development of Piezoelectric Coaxial Filament Sensors P(VDF-TrFE)/Copper for Textile Structure Instrumentation. *Sens. Actuators, A* **2013**, *204*, 122−130.

(25) Hou, R.; Fu, Y. Q.; Hutson, D.; Zhao, C.; Gimenez, E.; Kirk, J. K. Use of Sputtered Zinc Oxide Film on Aluminium Foil Substrate to Produce a Flexible and Low Profile Ultrasonic Transducer. *Ultrasonics* **2016**, *68*, 54−60.

(26) Takenaka, T.; Nagata, H. Current Status and Prospects of Lead-free Piezoelectric Ceramics. *J. Eur. Ceram. Soc.* **2005**, *25*, 2693−2700.

(27) Zgonik, M.; Bernasconi, P.; Duelli, M.; Schlesser, R.; Gunter, P.; Garrentt, M. H.; Rytz, D.; Zhu, Y.; Wu, X. Dielectric, Elastic, Piezoelectric, Electro-Optic, and Elasto-Optic Tensors of $BaTiO_3$ Crystals. *Phys. Rev. B* **1994**, *50*, 5941.

(28) Choi, K. J.; Biegalski, M.; Li, Y. L.; Sharan, A.; Schubert, J.; Uecker, R.; Reiche, P.; Chen, Y. B.; Pan, X. Q.; Gopalan, V.; Chen, L. Q.; Schlom, D. G.; Eom, C. B. Enhancement of Ferroelectricity in Strained $BaTiO_3$ Thin Films. *Science* **2004**, *306*, 1005−1009.

(29) Li, W.-W.; Zhang, W.; Wang, L.; Gu, J. X.; Chen, A.; Zhao, R.; Liang, Y.; Guo, H.; Tang, R. J.; Wang, C.; Jin, K.; Wang, H.; Yang, H. Vertical Interface Induced Dielectric Relaxation in Nanocomposite $(BaTiO_3)_{1-x}$:$(Sm_2O_3)_x$ Thin Films. *Sci. Rep.* **2015**, *5*, No. 11335.

(30) Harrington, S. A.; Zhai, J.; Denev, S.; Gopalan; Wang, H.; Bi, Z. X.; Redfern, S.; Baek, S.; Bark, C.; Eom, C.; Jia, Q.; Vickers, M.; MacManus-Driscoll, J. L. Thick Lead-free Ferroelectric Films with High Curie Temperatures Through Nanocomposite-induced Strain. *Nat Nanotechnol.* **2011**, *6*, 491−495.

(31) Li, W.-W.; Zhao, R.; Tang, R.; Chen, A.; Zhang, W.; Lu, X.; Wang, H.; Yang, H. Vertical-Interface-Manipulated Conduction Behavior in Nanocomposite Oxide Thin Films. *ACS Appl. Mater. Interfaces* **2014**, *6*, 5356−5361.

(32) Zhang, X. Y.; Xu, R. X.; Gao, X. Y.; Li, M.; Shi, X.; Ji, Y.; Qian, F.; Wang, H.; Li, W.-W.; Yang, H.; et al. Achieving Ohmic Conduction Behavior at High Electric Field via Interface Manipulation. *Appl. Surf. Sci.* **2020**, *516*, No. 146093.

(33) Xu, R. X.; Li, M.; Qi, Z.; Zhang, X.; Jian, J.; Ji, Y.; Qian, F.; Fan, J.; Kan, C.; Wang, H.; Tian, W.; Li, L.; Li, W.-W.; Yang, H. Perovskite Transparent Conducting Oxide for the Design of a Transparent, Flexible, and Self-Powered Perovskite Photodetector. *ACS Appl. Mater. Interfaces* **2020**, *12*, 16462−16468.

(34) Yang, Y.; Yuan, G.; Yan, Z.; Wang, Y.; Lu, X.; Liu, J. Flexible, Semitransparent, and Inorganic Resistive Memory Based on $BaTi_{0.95}Co_{0.05}O_3$ Film. *Adv. Mater.* **2017**, *29*, No. 1700425.

(35) Jiang, J.; Bitla, Y.; Huang, C.; Do, T.; Liu, H.; Hsieh, Y.; Ma, C.; Jang, C.; Lai, Y.; Chiu, P.; Wu, W.; Chen, Y.; Zhou, Y.; Chu, Y. Flexible Ferroelectric Element Based on van der Waals Heteroepitaxy. *Sci. Adv.* **2017**, *3*, No. 1700121.

(36) Wu, J.; Liang, Z.; Ma, C.; H, G.; Shen, L.; Sun, Z.; Zhang, Y.; Lu, L.; Liu, M.; Jia, C. Flexible Lead-Free $BaTiO_3$ Ferroelectric Elements with High Performance. *IEEE Electron Device Lett.* **2019**, *40*, 889.

(37) Munro, R. G. Elastic Moduli Data for Polycsystalline Ceramics 6853 (NISTIR, 2002).

(38) IEEE Proceedings of the 5th International Symposium on Micro Machine and Human Science 75 (Nagoya, 1994).

(39) Wu, H.; Ma, X.; Zhang, Z.; Zeng, J.; Wang, J.; Chai, G. Effect of Crystal Orientation on the Phase Diagrams, Dielectric and Piezoelectric Properties of Epitaxial $BaTiO_3$ Thin Films. *AIP Adv.* **2016**, *6*, No. 015309.

(40) Zhang, X. Y.; Xu, R. X.; Gao, X. Y.; Ji, Y.; Qian, F.; Wang, H.; Li, W.-W.; Yang, H.; et al. Negative-pressure Enhanced Ferroelectricity and Piezoelectricity in Lead-free $BaTiO_3$ Ferroelectric Nanocomposite Films. *J. Mater. Chem. C* **2020**, *8*, 8091−8097.

(41) Kursumovic, A.; Defay, E.; Lee, O.; Tsai, C.; Bi, Z.; Wang, H.; MacManus-Driscoll, J. A New Material for High-Temperature Lead-Free Actuators. *Adv. Funct. Mater.* **2013**, *23*, 5881.

(42) Sohn, H.; Park, G.; Wait, J. R.; Limback, N. P.; Farrar, C. R. Wavelet-based Active Sensing for Delamination Detection in Composite Structures. *Smart Mater. Struct.* **2004**, *13*, 153.

(43) Worden, K.; Pierce, S. G.; Manson, G.; Philp, W. R.; Staszewski, W. J.; Culshaw, B. Detection of Defects in Plates Using Lamb Waves and Novelty Detection. *Int. J. Syst. Sci.* **2000**, *31*, 1397.

(44) Lemistre, M.; Balageas, D. Structural Health Monitoring System Based on Diffracted Lamb Wave Analysis by Multiresolution Processing. *Smart. Mater. Struct.* **2001**, *10*, 504.

(45) Wang, Y.; Qiu, L.; Luo, Y.; Ding, R. A Stretchable and Large-scale Guided Wave sensor Network for Aircraft Smart Skin of Structural Health Monitoring. *Struct. Health Monit.* **2021**, *20*, 861−876.

(46) Gannepalli, A.; Yablon, D. G.; Tsou, A. H.; Proksch, R. Corrigendum: Mapping Nanoscale Elasticity and Dissipation Using Dual Frequency Contact Resonance AFM. *Nanotechnology* **2003**, *24*, No. 159501.

(47) Harnagea, C.; Pignolet, A.; Alexe, M.; Hesse, D.; Gösele, U. Quantitative Ferroelectric Characterization of Single Submicron Grains in Bi-layered Perovskite Thin Films. *Appl. Phys. A: Mater. Sci. Process.* **2000**, *70*, 261−267.